Experimental Study and Analysis of Ice Crystal Accretion on a Gas Turbine Compressor Stator Vane

Author, co-author (Do NOT enter this information. It will be pulled from participant tab in MyTechZone)

Affiliation (Do NOT enter this information. It will be pulled from participant tab in MyTechZone)

Abstract

A significant number of historical engine powerloss events have recently been attributed to ingestion of high altitude ice crystals, prompting regulators to expand engine certification envelopes to incorporate 'ice crystal icing' conditions. There has been a resulting effort by OEMs and academia to develop analytical and semi-empirical models for the phenomenon, partly through use of rig testing. The current study presents results and analysis of experiments conducted in the National Research Council's Research Altitude Test Facility (RATFac). The experiments used a simplified compressor stator vane test article, designed to produce data to build semi-empirical models and validate an existing ice crystal icing code. Accretion growth rates, extracted from backlit shadowgraphy, are presented as a function of test condition, and the algorithm of a new image processing technique using Canny filtering is discussed. Wet bulb temperature, Mach number, particle size and test article angle of attack were systematically varied. In line with previous experiments, the accretion growth rate was observed to be strongly dependent upon bulk particle melt ratio, with a peak growth rate at approximately 10% melt ratio. If leading edge accretions shed during the test, the growth rate of the second accretion would be greater than the first, regardless of test condition, due to the cooling of the substrate surface during the first accretion. The rate of erosion was found to correlate with bulk particle kinetic energy. The highest growth rates were observed for positive angles of attack, at both the leading edge and pressure surface. In contrast, at negative angles of attack growth rates were minimized, attributed to unfavourable accretion conditions on the suction surface. Finally, a qualitative assessment of the accretion quality and build/shed behavior as a function of test condition is presented.

Introduction

Over 240 icing-related engine powerloss events have been recorded since 1990, with a significant proportion occurring at altitudes in excess of 7000 m, the approximate upper limit at which water can exist in supercooled liquid form. Mason et al [1] studied 46 of these events, attributed to the accretion of solid ice crystals in the engine core compression system. This phenomenon, more generally known as 'ice crystal icing', has caused loss of power (rollback), blade damage, flameout and surge. The recent release of new regulatory envelopes by the FAA and EASA, designed to fully incorporate ice crystal icing conditions, has spurred efforts to develop analytical and semi-empirical models for the phenomenon as an acceptable means demonstrating safe operation.

At the University of Oxford, a new numerical model, termed the Ice Crystal Icing ComputationaL Environment (ICICLE) has been developed. It incorporates particle size and shape treatment, Lagrangian particle tracking, heat transfer and phase change, stick, bounce and shatter models, and a thermodynamic accretion model based on the Extended Messinger Model. A full description of the model may be found in [2]. Models for sticking efficiency and erosion were developed from experimentation on a cone test article [3]. To validate the complete model, datasets from independent experiments were required. Several experimental campaigns have been conducted in recent years to build datasets for ice crystal icing on simple geometries such as cones and hemispheres [4], symmetrical aerofoil and wedge sections [5] and intercompressor ducting [6], [7]. Compressor stator vanes have been tested as a cascade, but it has been observed that significant ice blockage in the vane passages can lead to image obscuration and may inhibit the extraction of quantitative data; however, qualitative insight may be attained. Stator vanes nevertheless are clearly of interest for modelling engine icing, particularly the leading edge and concave pressure surface where large accumulations may be expected. An ability to correctly model particle catch and bounce on these continuously curving surfaces is a necessary precursor to more complex, and/or 3D geometries.

Determination of ice growth rates, sticking efficiencies and erosion rates has typically relied on video shadowgraphy to track the accretion profile over time. This in turn relies on a robust post-processing code to detect the edge of the accretion profile in each video frame. The noise in the output depends on the image quality, the obscuration of the test article (whether by the icing cloud or ice on the window), and the particular edge detection algorithm used. Struk & Lynch [8] presented an edge detection method and uncertainty analysis framework, applied to ice accretion on a wedge aerofoil at an arbitrary angle of attack. NASA's Spotlight image analysis package was used, which uses a Sobel filter to detect and amplify strong intensity gradients – indicative of edges. It was desired in the current study to use similar methods to improve an in-house code used in previous experiments [3], which uses pixel intensity – rather than intensity gradient – to find edges.

The objectives for the current study are therefore threefold. Firstly, to provide data on ice crystal accretion growth rates on a simplified compressor stator geometry, for modelling and validation. Secondly, to improve qualitative understanding of build and shed behaviour as a function of test condition; and thirdly to improve the signal-to-noise ratio in image post-processing techniques through application of new filtering algorithms.

Test Facility, Conditions & Test Article

Test Facility

The test facility used in the study was the Research Altitude Test Facility (RATFac) at the National Research Council of Canada (NRC), Ottawa. The facility, developed continuously since 2006, comprises a wind tunnel and ice particle generation system, housed in an altitude chamber. A schematic of the facility is shown in Fig. 1. The chamber is divided into a 'cold' section, where an ice grinder produces particles of a target Particle Size Distribution (PSD) at sub-freezing temperatures. These are then fed in the ice injection pipe to the 'warm' part of the chamber, which is maintained at a target total temperature. The particles are fed as a free jet into the bellmouth of the wind tunnel – known as the cascade rig – mixed with any supplemental liquid water from a spray mast. The wet bulb temperature in the test section may be controlled by varying the total

© Copyright Rolls-Royce Plc 2019. All rights reserved. UK Origin Material, Export Control: not Export Controlled

temperature, total pressure and/or humidity, the latter controlled by steam injection. Heated windows are available to image the test article from side, top or isometric perspectives. More detail on the facility commissioning and its previous campaigns is available in [6], [9], [10].

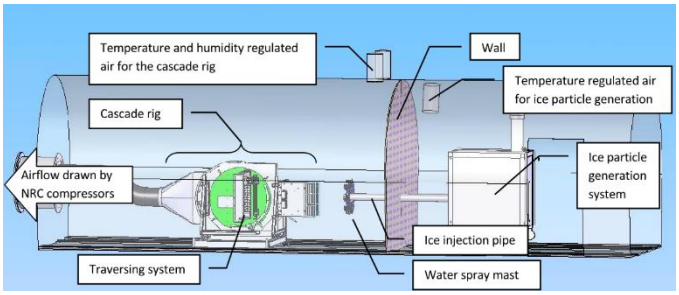


Fig. 1 Schematic of the cascade rig in RATFac [10]

Test Conditions

A total of 39 test points were completed with the test article in-situ, and an additional 14 cloud calibration tests with the test article absent. In all tests, the mixed phase icing cloud was generated by natural melt of initially glaciated particles in a warm airstream, as opposed to by supplemental liquid water injection.

A summary of the conditions tested is given in Table 1. Total pressure was held at 34.5 kPa (ISA altitude of approximately 8.2 km / 27,000 ft) and total air temperature (TAT) at 10 °C. Aerodynamic conditions were obtained indirectly when ice was flowing by measuring parameters (total pressure, and total and static temperature) pre-test and superimposing the change in each parameter provided by probes designed to operate in an icing cloud (including the downstream-facing TAT-RH probe).

Table 1 Summary of test conditions

Parameter	*Minimum*	*Baseline*	*Maximum*
Mach [-]	0.25	0.40	0.40
Relative humidity [-]	0.05	0.22	0.65
TWC [g/m^3]	4.0	8.0	12.0
Ice D_{v50} [µm]	34	34	68
Angle of attack [°]	-20	0	20

Test Article

The test article was a compressor stator vane, as shown in Fig. 2 (a). This was chosen to be pertinent to engine icing, albeit heavily simplified compared to a 'real' engine stator vane. The blade profile selected was representative of that in an intermediate pressure compressor. The aspect ratio, defined as the ratio of span to true chord, was 2.1, and the blade camber angle was 28°. The stator was mounted into a circular polycarbonate window, which itself was mounted into a rotatable frame, allowing angle of attack variation. The stator suction surface and the circular window are shown in Fig. 2 (b). There was a ~ 30 mm gap between the tip and window to prevent ice buildup obscuring the image. Since the ice concentration decreases near the tunnel walls, the gap also ensured that the tip and midspan region were exposed to the icing cloud core. The side view of the tip is shown in Fig. 2 (c).

The test article was machined from a titanium alloy, typical of the material used in the compressor of modern civil gas turbines. The as-machined surface roughness was approximately equal to an entry-into-service condition, measured using a Taylor-Hobson Surtronic 3+ profiler, with an accuracy of 2% of the reading.

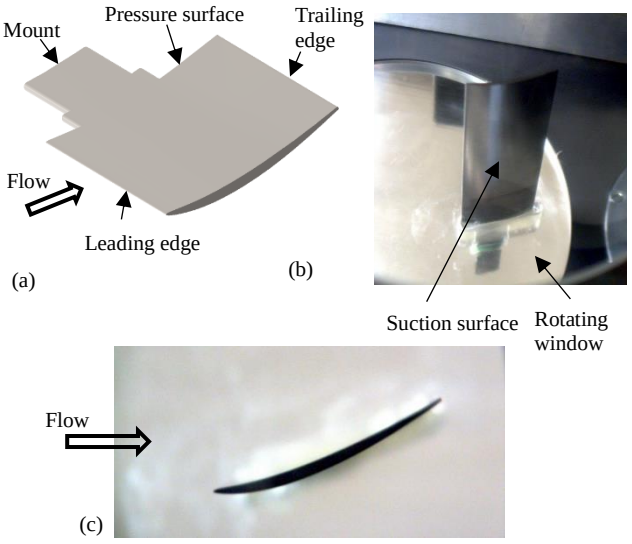


Fig. 2 Isometric view of stator test article; (b) suction surface view and (c) side (tip) view of the stator installed in RATFac. Flow is left to right in all images.

CFD simulations using ANSYS Fluent were used to aid test article design and to provide particle collection efficiency data around the aerofoil surface. Fig. 3 shows contours of normalised velocity at the baseline aerodynamic condition. Details on the mesh and numerical setup are given in Appendix A.

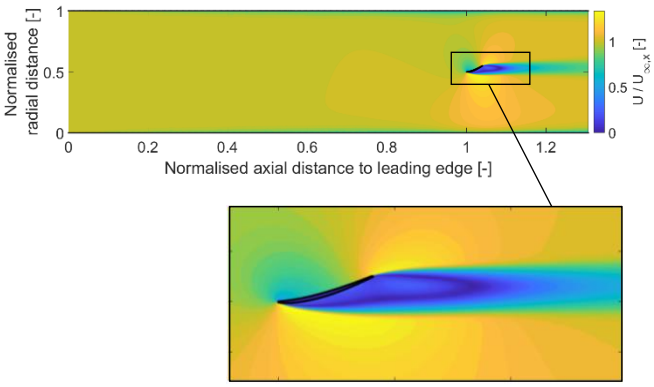


Fig. 3 Contours of velocity normalised by inlet freestream axial velocity; flow is left to right.

Since the stator is isolated (i.e. not in a cascade), it acts more as a bluff body, with early suction surface separation. This is not believed to be limiting for ice growth rate measurements since the leading edge and pressure surface are unaffected. Provided the flowfield and particle tracks can be predicted, then the stator can generate quantitative data for the geometric features of interest. This provides data with which to build semi-empirical models, and validation cases at a mid-fidelity level. Validation data from more realistic engine geometries – e.g. cascade or compressor module – may then follow with increased confidence.

Icing Cloud Calibration & Measurement

Particle Size Distribution (PSD)

The PSD was measured in-situ for selected tests using a Particle Imaging Velocimetry (PIV) system configured for backlit shadowgraphy. This was placed in between the ice grinder ejection

pipe and the inlet bellmouth of the cascade rig. The four nominal PSDs used in the campaign are given in Table 2.

Table 2 Size statistics for the four nominal PSDs used

Designation	D_{v10} *[µm]*	D_{v50} *[µm]*	D_{v90} *[µm]*
PSD 1 (baseline)	18	34	54
PSD 2	25	40	80
PSD 3	28	50	93
PSD 4	35	68	131

Total Water Content (TWC)

The TWC at the tunnel centerline was measured using the NRC Compact Iso-Kinetic Probe (CIKP) [11]. This probe evaporates the ingested mixed phase stream and uses the change in specific humidity to calculate the freestream TWC. Prior to each test, the ice feed rate was adjusted until the centerline TWC, $TWC_{cl,CIKP}$, was approximately equal to the target value. The ice feed was then ceased, the CIKP retracted and the test article de-iced, before the ice flow was restarted to begin the test.

Liquid Water Content (LWC)

LWC was measured pre-test using the Science Engineering Associates WCM-2000 multiwire probe [12]. Originally designed for operation in supercooled liquid water droplet conditions, the response of this probe in mixed phase conditions is an area of active research [4], [5]. In fully glaciated conditions, the probe gives a spurious LWC reading due to particles bouncing off the heated wires, termed the 'false response'. This was parametrically characterized as a function of test condition in [3], yielding the following empirical relationship:

$$FR\ (\%) = a + \frac{M - 0.4}{0.017\ D_{v50} + 0.243} TWC_{cl,CIKP} \qquad (1)$$

where the constant a is given in Table 3.

Table 3 Determined values of model constant 'a'

Mach [-]	D_{v50} *[µm]*	*Value of a [-]*
0.25	34	3.75
0.25	40	3.79
0.40	34	3.79
0.40	40	4.70

The bulk melt ratio at the tunnel centerline, corrected for the false response, may then be estimated from

$$MR_{corr}\ (\%) = \frac{\max\left(LWC_{multi,1}, LWC_{multi,2}\right)}{\beta_{MW} TWC_{cl,CIKP}} - FR \qquad (2)$$

where $multi,1$ and $multi,2$ refer to the LWC readings from each of the two sensing wires in the SEA multiwire probe, and FR is given by equation (1). β_{MW} is the collection efficiency of the multiwire sensing wires. This will be less than unity for the smallest (streamline-following) particles. It is estimated from [13] as ~0.94 for PSD 1, ~0.97 for PSD 2, and unity for PSDs 3 and 4. Struk et al [13] also present a correction to account for the water-sensing wires under-reporting LWC in a fully liquid cloud, when compared to the CIKP. This correction is neglected here since it will dominate at high melt ratios (the highest tested here using natural melt believed to be ~ 20%) and additionally has not been calibrated for use in mixed phase conditions generated by natural melting.

Since the response of the probe cannot be calibrated by an independent device over the range used in this test, a reasonable estimate of bias (systematic) uncertainty in LWC measurement cannot be made. Given these limitations, the absolute value of MR_{corr} quoted should be viewed with caution.

Ice Growth Measurement & Processing

Imaging

The stator was backlit through the rotating side window and the free end (tip) imaged from a window on the opposite side of the tunnel. A 5.0 megapixel Avigilon 5.0MP-HD-DN video camera (2592 x 1944 resolution, 5 fps frame rate) was used. Additional cameras provided a top-down view of the pressure surface, and an isometric view of the test article for qualitative assessment of the ice growth and spanwise uniformity.

Image Processing

To calculate the ice growth rate at a given location on the test article, the outline of the ice accretion must be located in each frame of video. This was performed in previous experiments [3] using an in-house video analysis code. A mask is created, encapsulating the final accretion profile to define the region of interest. The mask comprises some 1000 vectors spaced around the article, normal to the surface. For each video frame, the greyscale intensity of all pixels along each vector is calculated. A root-mean-square difference method is used to find the largest step-change in greyscale intensity, isolating the accretion edge – if there are no spurious stronger edges in the image.

It was observed that the signal-to-noise ratio of this method could, under certain conditions, become unacceptably high. This would occur near the test start, where accretions were thin, patchy and more translucent; also at test conditions where the icing cloud was most 'opaque' – corresponding to low melt ratio particles (i.e. lower wet bulb temperatures), and a high TWC. It was determined that the signal noise in these conditions could be reduced by basing the edge detection on intensity *gradient*, as opposed to an absolute value.

A Canny edge detection algorithm [14] was selected as the preferred method of edge detection for this study, implemented in a MATLAB library function.

The steps in the algorithm may be summarized as:

1. Each frame is converted to greyscale.
2. Spurious edge detection may arise from image noise. A Gaussian smoothing filter is created and convolved with the image to locally blur the image.
3. The gradient in pixel intensity is calculated at each pixel location. The Canny filter improves on a one-dimensional intensity gradient method by applying a Sobel convolution technique across the image, which resolves the intensity gradient in Cartesian co-ordinates [14].
4. Edges, blurred by the Gaussian filter, must now be 'thinned'. For each region of high gradient change, denoting an edge, the pixel with the largest gradient in intensity is sequentially searched for. Any pixels with gradients less than the current highest value are given a null value. This is known as non-maximum suppression. There is necessarily some manual tuning of the non-maximum suppression threshold as a result of test-to-test variations in backlighting intensity, and window and cloud obscuration of the test article.
5. 'Weak' edges, with the lowest gradients in intensity, might be associated with real edges in the image, or may be noise or colour artefacts. It is assumed that in the former case, weak edge pixels are in close proximity to

strong edge pixels. A hysteresis double thresholding process is therefore used. This identifies strong edges with intensity gradients above the threshold and weaker edges that are (i) between the strong and weak threshold values and (ii) are connected to strong edges. If there is a strong edge within the nearest eight neighboring pixels, a physical edge is assumed [14].

6. The ice edge is constructed using a cubic spline to connect pixels identified as edges. For especially noisy image frames, multiple edges may be identified near a given physical location. To mitigate this, a moving average filter was used to smooth edges over five consecutive image frames.

Fig. 4 shows a comparison of ice accretion at the test end and the detected edge profile using the Canny filter, before the final profile spline is added. An edge has been detected from a blurred shape out of the focal plane of the camera – likely the edge of an ice lump on the opposing (backlit) window. This is removed by the median-filtered fitted spline. In future tests, it would be desired to improve how the backlit window is heated to avoid these accretions. An example of the final detected profile is shown in Fig. 5 at three test times for a test at an angle of attack of +10°.

At discrete timepoints of each test, the standard deviation in the measured thickness near a fixed location was used to obtain an estimate of precision uncertainty. This proved to be highly dependent on test condition, with the combined precision and bias uncertainty estimated to be +/-1.0 mm in the worst case. A full uncertainty analysis is given in Appendix B.

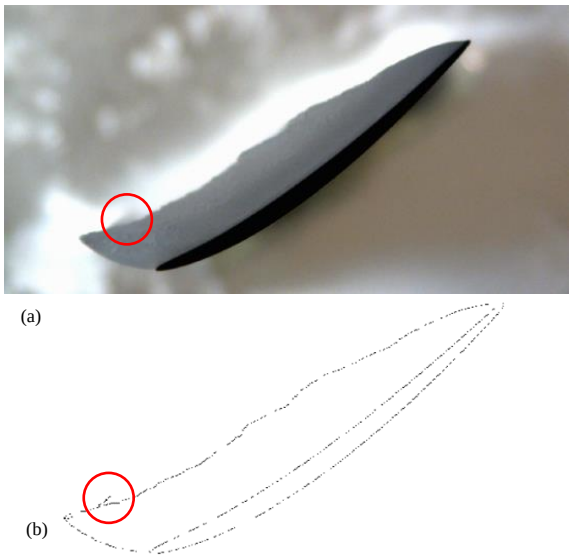


Fig. 4 Comparison of (a) image of ice accretion and (b) edge detection using the Canny filter. Circled in red – detection of an edge out of the focal plane of the camera.

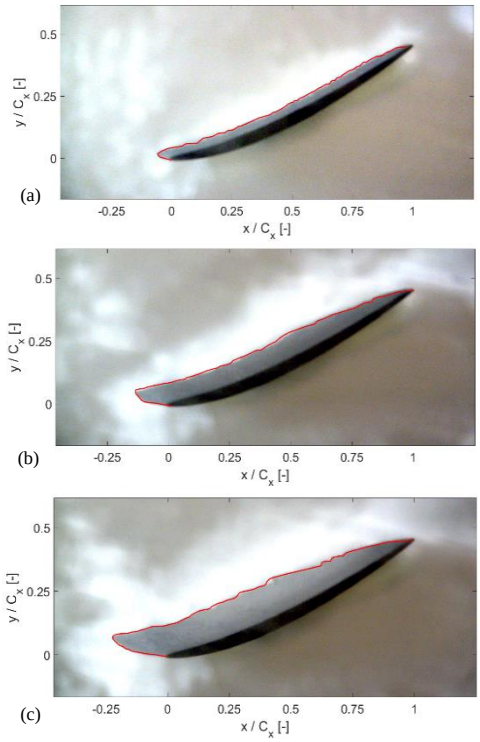


Fig. 5 Ice accretion and detected profile edge after (a) 33% test duration, (b) 66% test duration, and (c) at test end. The case is +10° angle of attack, TWC = 4 g/m^3; all other conditions are at their baseline values.

Sticking Efficiency Calculation

A 'net' sticking efficiency is defined as the fraction of the impinging mass flux that sticks less the fraction that bounces or is eroded. This may be calculated from the local thickness growth rate $\dot{h}_{loc}$ as follows:

$$\eta_{s,net} = \frac{\dot{m}_{acc}}{\dot{m}_{imp}} = \frac{\dot{h}_{loc}\,\rho_{acc}}{\beta_{loc}\,\dot{m}_{\infty,loc}} = \frac{\dot{h}_{loc}\rho_{acc}}{\varepsilon_{loc}\cos\gamma\,TWC_{loc}\,U_{\infty}} \qquad (3)$$

where $\dot{m}_{\infty,loc}$ is the local impinging mass flux. The local average particle collection efficiency, β_{loc}, may be expressed as $\varepsilon_{loc}\cos\gamma$, where ε_{loc} is a ballistic efficiency (equal to unity for entirely ballistic particles) and γ is the angle between the local surface normal and axial directions. A distribution of β_{loc} was calculated using Lagrangian particle tracking in the commercial CFD package Ansys FLUENT v16.2, for each of the four PSDs and two Mach numbers. Fig. 6 shows the distribution of collection efficiency around the stator surface, when at 0° angle of attack, at the baseline aerodynamic and particle size condition.

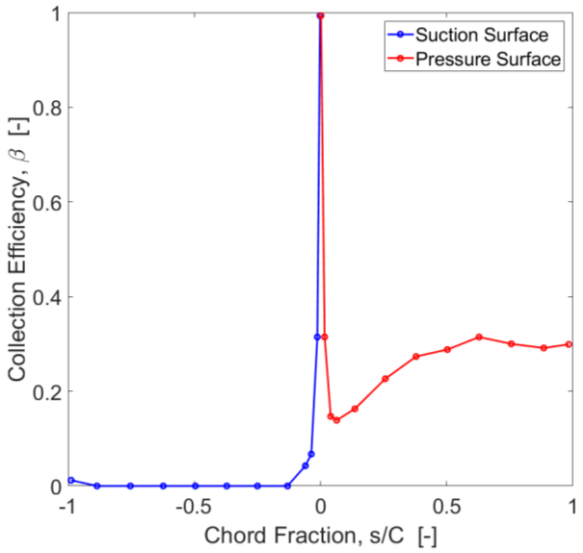


Fig. 6 Collection efficiency distribution on the stator at 0° angle of attack at the baseline aerodynamic and particle size condition.

The PSDs were converted to equivalent Rosin-Rammler distributions. Details of the discrete phase parameters are given in Appendix A. The drag coefficient correlation of Haider & Levenspiel [15] for non-spherical particles was selected, using a mean particle aspect ratio found during particle morphology studies in RATFac [16]. For simplicity, the values of β_{loc} are assumed to remain constant over the accretion time.

Uncertainty Analysis

An uncertainty analysis is given in Appendix B. As discussed above, the absolute uncertainty in accretion thickness was dependent upon test condition, but estimated to be +/-1.0 mm in the worst case. The uncertainty in net sticking efficiency, $\eta_{s,net}$, is calculated using a root-sum-squares method. The absolute uncertainty is estimated as +/- 0.15 in the worst case.

Results

Effect of Varying Relative Humidity

Varying relative humidity at fixed temperature and pressure permits a variation in wet bulb temperature, and hence in the rate of melting of the initially glaciated particles. It has been observed in previous ice crystal icing experiments that particle sticking efficiency is strongly dependent upon bulk melt ratio [3], [4], [10]. At low values – typically below 5% - there is insufficient water for particles to stick (provided particle-surface heat transfer is small), whereas at melt ratios in excess of ~ 30%, splashing, filming and sliding inhibit sticking.

Relative humidity – based on total conditions – was varied between 5% and 65% at a constant total temperature of 10 °C, total pressure of 34.5 kPa and Mach number of 0.40. Angle of attack was held at 0°, TWC at 8 g/m^3 and particle D_{v50} at 34 µm. The humidity sweep in turn varied the total wet bulb temperature in the range -6.5 °C to 5.5 °C, with a corresponding range of bulk particle melt ratios. For two tests, the total temperature was raised to 20 °C, and the relative humidity adjusted down to match the two highest total wet bulb temperatures: 2.5 °C and 5.5 °C.

Fig. 7 shows normalised sticking efficiency at the stator leading edge against bulk melt ratio. For the higher humidity tests, accretions were generally more slushy, less well anchored to surfaces and more prone to shed. For these cases, the growth rate up until the first shed (the 'first growth') and the subsequent growth until the next shed (the 'second growth') were recorded. It has been demonstrated in previous studies [17] that the growth rate may be materially different between the first and second growths, attributed to surface cooling during the first growth reducing melting and water film development in the second growth.

All data are normalised against the maximum sticking efficiency at the TAT = 10 °C condition. Error bars are plotted for the first growth data at TAT = 10 °C. For the reasons given in the discussion of the multiwire probe, the uncertainty in MR_{corr} cannot be estimated.

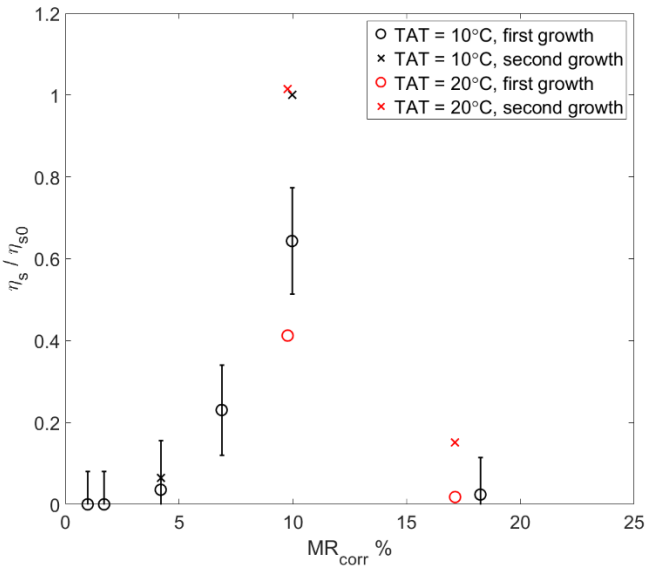
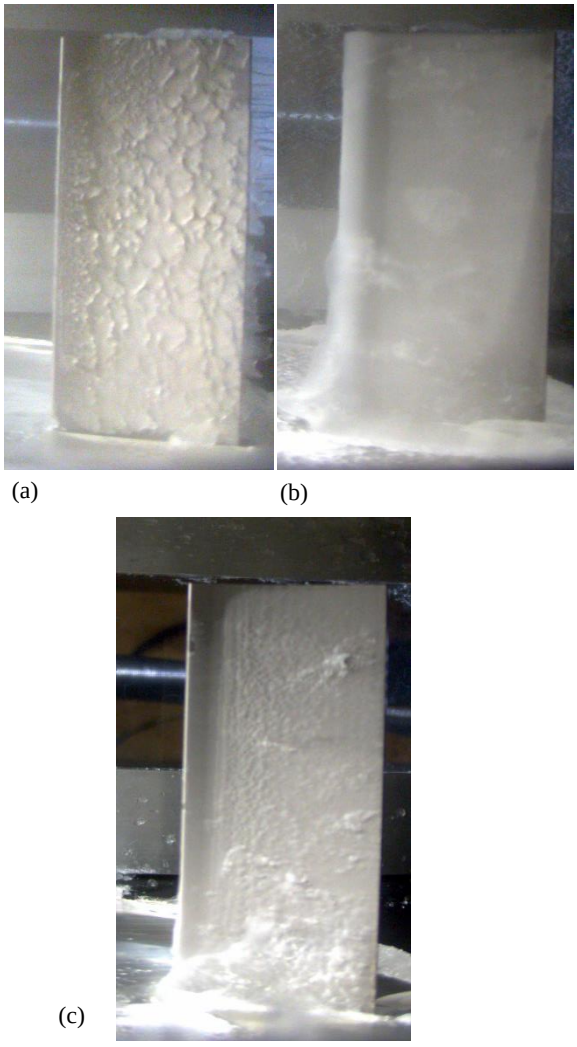


Fig. 7 Normalised sticking efficiency at the stator leading edge for relative humidity in the range 5% - 65%, and 10 °C and 20 °C total temperature (TAT). All other conditions were at their baseline values.

The data for the first growth at TAT = 10 °C show an increase in sticking efficiency up to a peak at a melt ratio of ~ 10 %, followed by a roll off down to almost zero growth at a melt ratio of ~ 18%. In previous experiments [3], which used a 35° half-angle cone as the test article, it was shown that the sticking efficiency peaks in a 'plateau region' of 9-13% melt ratio, irrespective of the Mach number and particle size. The trend exhibited in the current data is clearly similar, although the roll-off is significantly steeper than the cone case, which was able to retain non-zero sticking efficiencies up to melt ratios of ~30 %. This is indicative of the effect of geometry on the accretion stability at the stagnation point of the test article – the tip of the cone and leading edge of the stator. Fig. 8 (a) shows a top-view image of the stator at a total wet bulb temperature of 5.5°C (corresponding to the highest melt ratio data points in Fig. 7). It can be seen that the leading edge accretion on the stator is negligible, despite some slushy accumulations on the pressure surface. At the same test condition on the cone test article, the tip and the relatively oblique sloping cone walls provided an anchor point for accretion. This demonstrates that the sticking efficiency of accretions at high melt ratio is somewhat geometry dependent, and re-iterates the importance of sliding and shedding models for accurate computational predictions. Fig. 8(b) shows the accretion at test-end for a relative humidity of ~ 30%, corresponding to a melt ratio of ~ 4%. The leading edge accretion is clearly visible and well anchored to the blade. Further discussion of shedding characteristics is given later. Fig. 8 (c) shows the accretion for a relative humidity of ~15%, corresponding to a melt ratio of ~2%.



(a) (b)

(c)

Fig. 8 Top views of the stator at a wet bulb temperature of (a) 5.5 °C, (b) -0.5 °C and (c) -3.5°C. All other conditions are at their baseline values.

Four datapoints are shown in Fig. 7 at the plateau-region melt ratio of ~10%. These correspond to the first and second growths at total temperatures of both 10 °C and 20 °C. At the 10 °C condition, the first growth has a normalized sticking efficiency of around 0.65 times that of the second growth; at the 20 °C condition this falls to a factor of ~0.4. This is to be expected since more surface melting and water filming will occur for a blade initially immersed in 20 °C air than 10 °C air. For the second growth, the normalized sticking efficiencies are matched within 2%. This suggests that the blade surface has been cooled to a similar point for both air temperature conditions. The data are not dissimilar to the findings of Struk et al [17], where ice was grown on a NACA 0012 aerofoil in RATFac. At a total temperature of 15 °C and a wet bulb temperature of 3.0 °C (0.5 °C higher than the condition considered here), the growth rate of the accretion before the first shed was ~40% of that of the second accretion.

Effect of Varying Mach Number & PSD

A model for mass loss from an accretion in ice crystal icing was proposed in [3]. This includes a term for ductile erosion, characterized by material removal due to glancing (tangential) particle impacts. It was determined the erosion rate was dependent upon a quasi- kinetic energy parameter, defined as $KE = \overline{D^3}U^2$, where $\overline{D^3}$ is calculated by cubing the particle diameter for each bin in the distribution and then taking a mass average. The net sticking efficiency is given by

$$\eta_s = P_s(1 - \eta_{ero}) \quad (4)$$

where P_s is the sticking probability. This is defined on a scale of zero to one, and is solely a function of melt ratio, as given in [3]. The erosive efficiency, η_{ero}, is related to the kinetic energy parameter KE by

$$\eta_{ero} \propto \left(1 + \log_{10}\left({KE}/{KE_0}\right)\right) \quad (5)$$

where an erosive efficiency of unity implies complete mass loss (i.e. no growth at all or a steady state accretion profile). To obtain a range of KE, the particle D_{v50} was varied in the range 34 µm - 68 µm, and freestream air velocities of 83 m/s and 132 m/s. To obtain 'true' KE values, particle tracking simulations in Ansys FLUENT were used to predict the slip velocity between particle and fluid at the test article plane. The computational setup is given in Appendix A. It was determined that the average slip velocity between air and particles at the test article plane was less than 2% of the freestream value for all size distributions, so was neglected. In all tests, the relative humidity, total temperature and total pressure were maintained at their baseline values.

Fig. 9 shows normalised sticking efficiency at the leading edge against equation (5). As predicted by equation (4), the sticking efficiency decreases proportionally until the particle kinetic energy is sufficiently high that no growth occurs. For cases with sporadic leading edge build-and-shed cycles, the highest recorded growth rate was used in Fig. 9. Due to the logarithmic term on the horizontal axis, errorbars are not shown; however the uncertainty in KE was less than 3% for all tests.

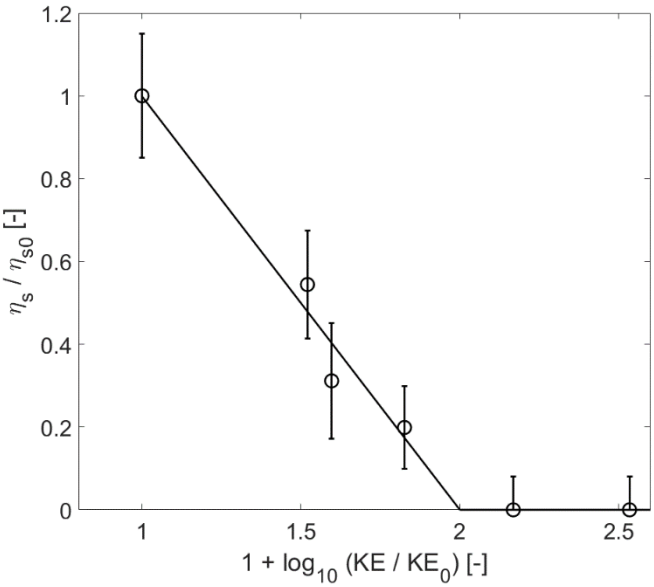


Fig. 9 Normalised sticking efficiency against equation (5), for tests with D_{v50} in the range 34-68 µm, and flow velocities of 83 and 132 m/s.

Fig. 10 shows two accretions at the test end, for (a) D_{v50} = 34 µm and (b) D_{v50} = 68 µm, both at a flow velocity of 132 m/s. At moderately-elevated particle kinetic energies (for example case (b)), pressure surface accretions were typically thin and patchy, initiating from the root, tip and/or the trailing edge. This is indicative that the flow structures in these locations are beneficial to particle sticking and accretion. Qualitatively similar behaviour was reported by Day et al. [18], where fine water droplets were ingested into a four-stage axial compressor. Water was observed to collect in the blade-endwall corner separation, as well as the trailing edge separation line. Fig. 10 (c) shows the same case as accretion (b) after 10% of the test duration, and (d) after 25% of the duration. Small, brittle leading edge accretions could also form, but were prone to shedding irregularly in small portions, as highlighted in Fig. 10 (b).

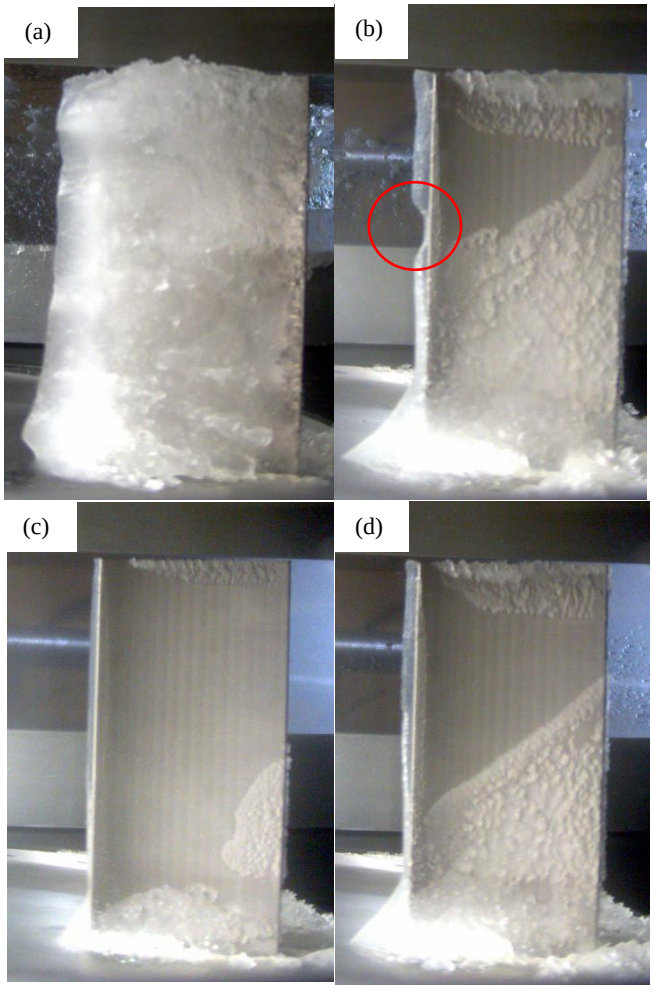


Fig. 10 Accretions at test end for (a) D_{v50} = 34 µm and (b) D_{v50} = 68 µm, and an elevated relative humidity of 45%. All other conditions were at their baseline values; flow is left to right. A partial leading edge shed is outlined in the red circle in (b). Image (c) shows the same case as accretion (b) after 10% test duration; (d) after 25% test duration.

Effect of Varying Angle of Attack

The vane angle of attack was varied between -20° and 20° in increments of 10°. All aerodynamic and icing conditions were at their baseline values. Fig. 11 shows accretions at test end for angles of attack of (a) -20°, (b) -10°, (c) 0°, (d) 10° and (e) 20°. Fig. 12 shows the average measured growth around the stator surface for each angle of attack, normalised by the growth rate at 0° angle of attack. In the case of -20° angle of attack, a full shed occurred after 87 s. The growth rate data is taken from the remainder of the test. The leading edge growth rate is taken as the maximum growth rate along any surface normal around the radius defining the edge.

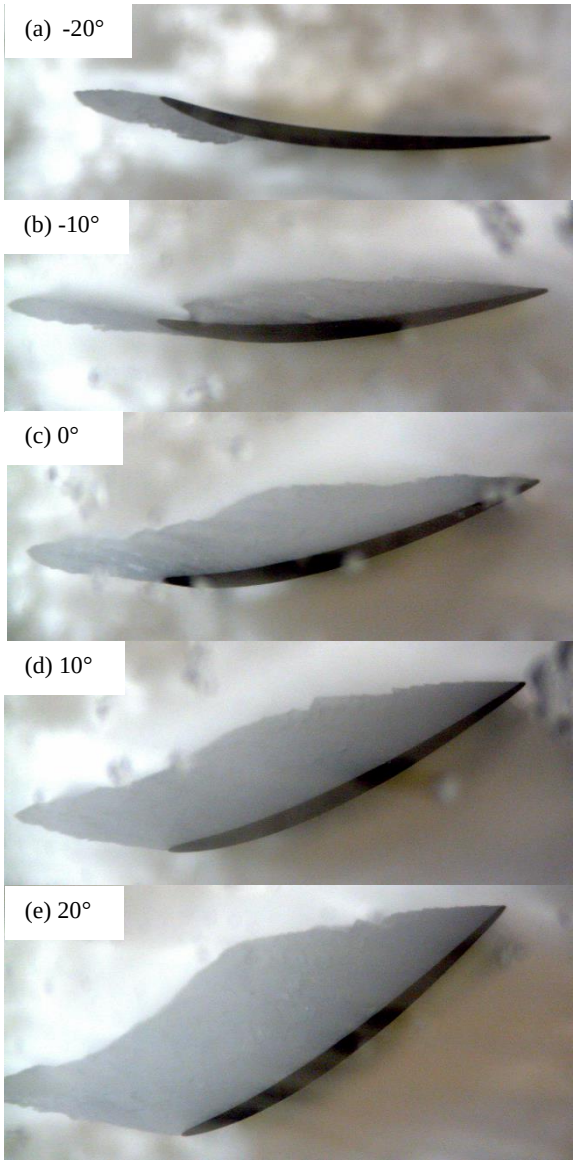


Fig. 11 Accretions at test end for angles of attack of (a) -20°, (b) -10°, (c) 0°, (d) 10° and (e) 20°. All test conditions were at their baseline values; flow is left to right.

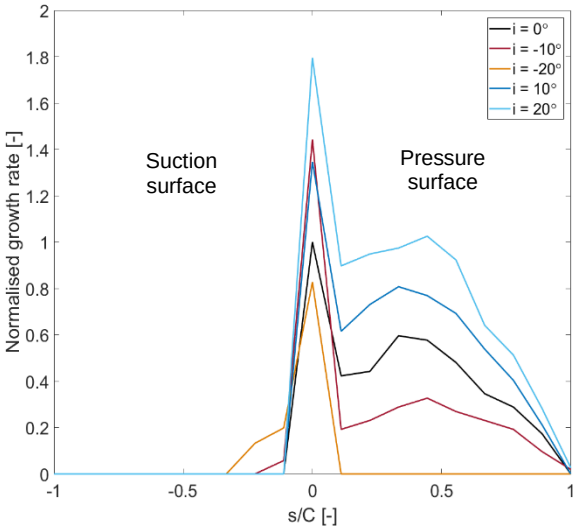


Fig. 12 Growth rate across the stator surface for angles of attack between -20° and 20°, normalised by the growth rate at 0° angle of attack.

On increasing angle of attack from 10° to 20°, the growth rate on the open face of the pressure surface scales approximately with the

increasing ballistic collection efficiency. For example, for a mid-chord position which has a surface normal of $\gamma = 75°$ to the axial direction when at zero angle of attack, the increase in collection efficiency is given by $\left({\cos(75-20)}/{\cos(75-10)}\right) = 1.36$. The average measured increase in growth rate on the pressure surface in the mid-chord region is ~ 1.4. The slightly higher measured value is attributable to an increased rate of erosion in the 10° case, where particle impacts are more oblique. It was shown in [3] that the rate of erosion could be correlated to $\sin^2\gamma$.

At an angle of attack of -10°, the first ~ 10% of the pressure surface in the chordwise direction has a surface normal of $\gamma > 90°$ relative to the axial direction – i.e. a leeward surface. In addition, a leading edge growth, partially anchored to the suction surface and angled slightly upwards from the axial direction acts to block this area from accretion. This persists until around 66% of the test duration, when the accretion on the remainder of the pressure surface gains sufficient height to be outside of the shadow zone of the leading edge accretion, and the accretion starts to grow forward towards the leading edge. Fig. 13 (a) shows the accretion at the 66% test duration and Fig. 13 (b) at test end. Note that these are top-down views of the same case as Fig. 11(b).

At an angle of attack of -20°, the pressure surface remains clear of any accretion for the test duration, save for a thin patch (< 2 mm thick) in the pressure surface – endwall corner. The first ~50% of the suction surface is exposed to the flow, though the convex surface and oblique impact angle promote a lower growth rate. The experiments of Guégan et al [19] showed that ice particle impacts with sufficient energy to induce fragmentation result in extremely oblique departure angles – typically less than 3°, albeit for larger particles (hail) than those tested here. Using the data in Hauk et al [20], fragmentation is expected at the baseline particle size and flow velocity. On a concave surface, therefore, multiple impacts of the same particle are likely, with the likelihood of sticking increasing as the particle loses kinetic energy. The convex suction surface therefore reduces the likelihood of this mechanism of sticking, and the flow acceleration around the early portion of the surface may promote particle sliding. As the surface normal approaches 90° to the axial at around mid-chord, the growth rate falls to zero, attributable to a near-zero collection efficiency and maximised erosion rate.

Overall it is worth noting that the growth rate is significantly reduced at negative angles of attack. This could potentially be used advantageously in compressor stages with variable geometry. An aerodynamic penalty will naturally be incurred, but this loss may be significantly outweighed by the aerodynamic penalty of larger pressure surface accretions. It is worth re-iterating that the aerodynamics are materially different from those encountered in an engine or cascade; the natural next step will be to test a cascade of variable geometry blades to determine if similar trends may be obtained.

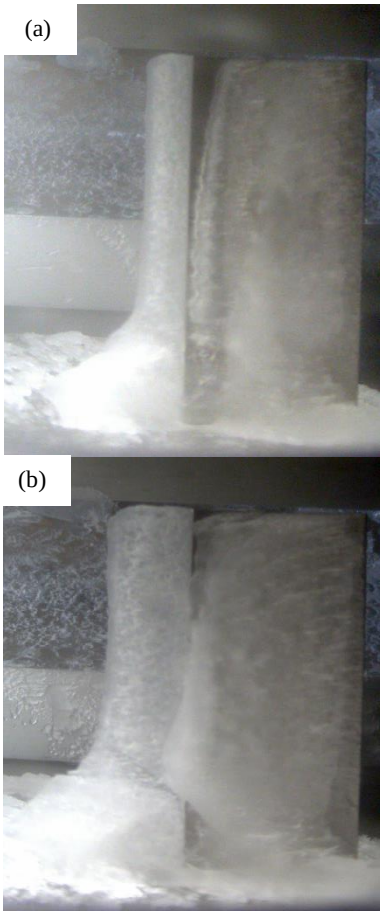


Fig. 13 Accretion at 66% test duration and 100% test duration for a test at -10° angle of attack. All other conditions are at their baseline values; flow is left to right.

Shedding

The propensity of accretions to shed, either partially or in entirety, was observed to be highly dependent upon test condition, most notably melt ratio. A qualitative assessment of shedding behaviour was performed, as shown in Fig. 14. Normalised particle kinetic energy and melt ratio were selected the parameters of interest. For each test, shedding frequency and primary location are shown. There is cluster of points where test conditions were held approximately constant and angle of attack was varied; these points are shown in more detail below the main figure.

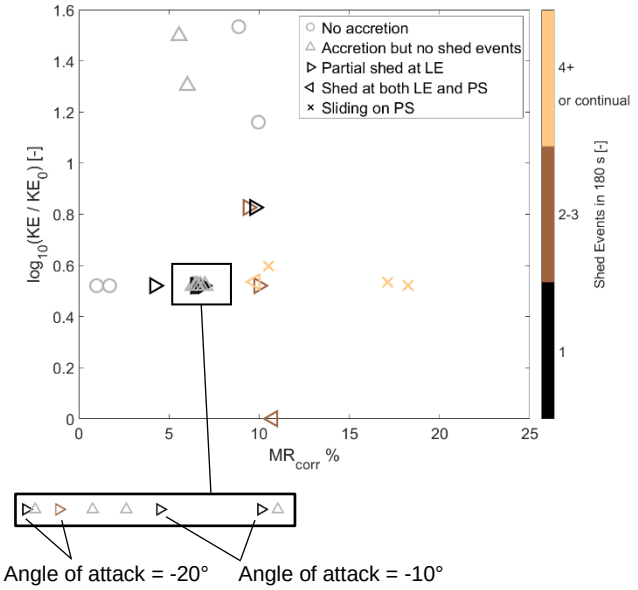


Fig. 14 Map of shedding frequency and type, as a function of melt ratio and normalised particle kinetic energy. Test points conducted at varying angle of attack inset.

It may be seen that shedding frequency increases at higher melt ratios, corresponding to slushy, poorly anchored accretions. Tests at melt ratios in excess of 15% led to regular or continual sliding of slushy sheets on the pressure surface. Fig. 15 shows accretions at (a) 16% test duration and (b) 50% test duration for a test at a melt ratio of ~ 17%. The accretions shown continually slid over the trailing edge and periodically shed. It may be seen that the maximum thickness only increases marginally between the two images. The near absence of leading edge accretions – which primarily serve as an anchor for the pressure surface accretion – further promotes sliding. When the leading edge is first exposed to the icing flow, it may be assumed that its temperature will approach the total wet bulb temperature – in this test +5.2 °C – and thus is more likely to remain free of accretion.

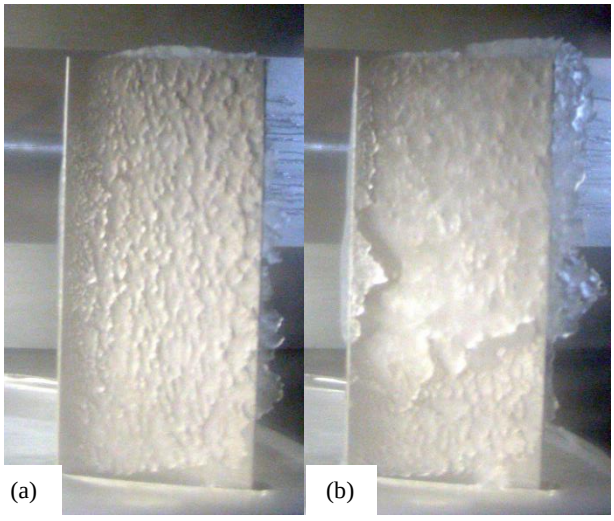


Fig. 15 Unstable accretions on the pressure surface at (a) 30 s and (b) 90s at a melt ratio of ~17%. All other test conditions were at their baseline values; flow is left to right.

This may be compared to cases at moderate melt ratios (~ 10%) where entire or partial shedding may occur semi-regularly (2-3 times per test). Fig. 16 shows accretions at various timepoints in a test at ~9.8% melt ratio, with all other baseline conditions. A leading edge accretion is visible in (a), at 30% test duration (TD), followed by a shed immediately after (b). More rapid growth ensues, particularly at the leading edge and near the root, as may be seen at 75% test duration (c). This is followed by a large shed immediately after (d), where the entire leading edge and around 40% of the span near the root (where the accretion, and thus drag force, was largest). Clearly this type of shedding has the potential to cause more damage to downstream components.

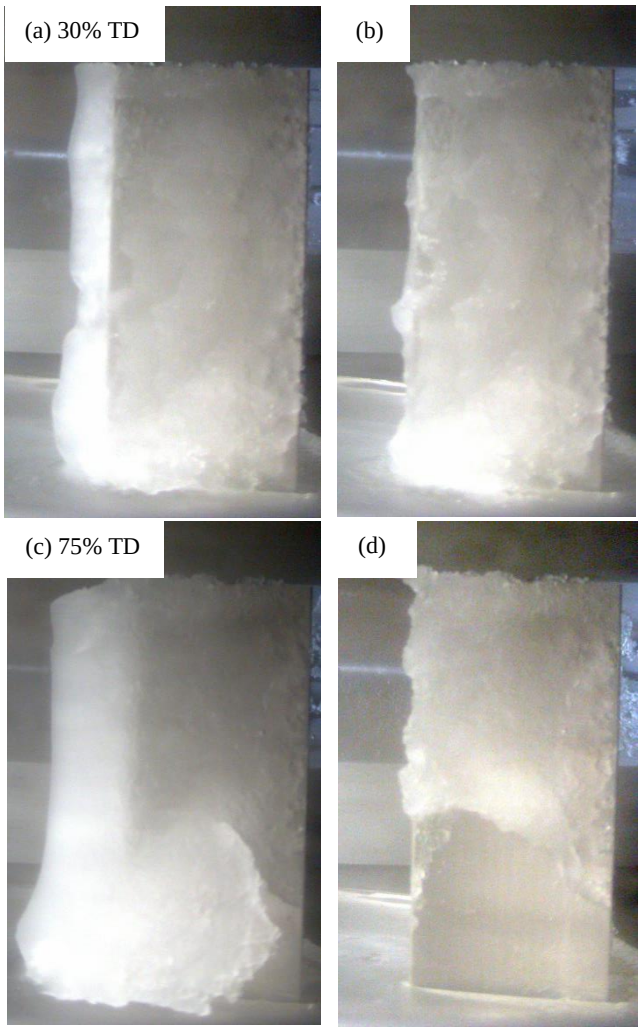


Fig. 16 Test at ~ 9.8% melt ratio after (a) 30% test duration (TD) and immediately after (b); (c) after 75% test duration and immediately after (d). All other conditions are at their baseline values; flow is left to right.

The most stable accretions only shed after the test end, when the flow of ice has been stopped. These accretions were typically hooked around the leading edge. After ice cessation, heat transfer from the suction surface to the pressure surface – the former recovering towards the freestream dry bulb temperature – warms the accretion bond on the pressure surface. The water layer between blade and accretion thickens, which visually may be observed by the accretion turning from opaque to translucent. At the point at which the aerodynamic forces on the accretion overcome the capillary force to the blade, the accretion may pivot about the leading edge - as shown in Fig. 17. Accretions were observed to remain in this position for over 30 s – whilst still in Mach 0.4 flow.

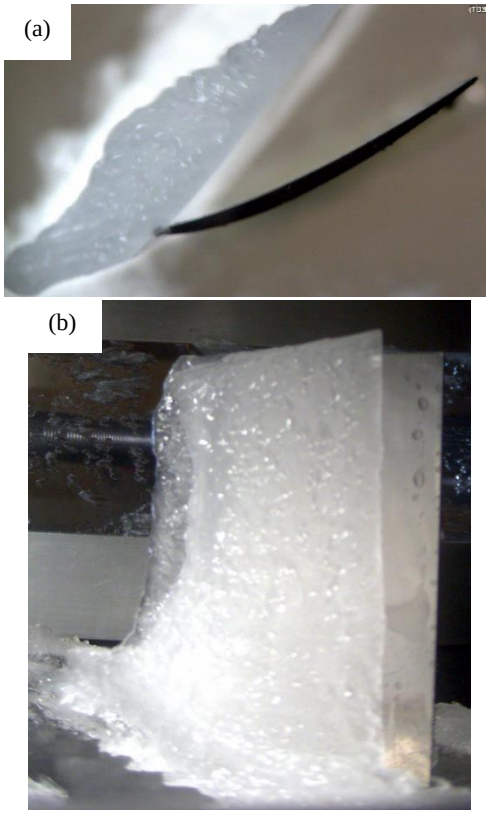


Fig. 17 Post-test rotation of entire accretion about the leading edge prior to shed, viewed from (a) the side and (b) the top; flow is left to right

The inset view of Fig. 14 shows the effect of varying angle of attack on shed type and frequency. It may be seen that the only tests with shedding were those at negative angles of attack of -10° and -20°, at or near the leading edge. Of the two tests at -20°, the higher melt ratio condition resulted in two sheds during the test time. At both negative angles of attack, the contact area between accretion and blade is small, in comparison to the area of the accretion exposed to the flow. Unlike on the concave pressure surface, the accretion has no anchor or support from the vane and is pulled underneath the suction surface. Operating at negative angles of attack therefore has a dual benefit – lower growth rates, and comparatively frequent shedding.

Conclusions

A stator vane test article was used in an ice crystal icing wind tunnel. It was designed to generate accretion profiles and growth rate data, aiding development and validation of a computational ice crystal icing model. The test article was chosen to be representative of a real engine component; a mid-way step between a fundamental geometry such as a cone or cylinder, and a full cascade or annulus sector. The results may be used to both validate existing codes, and tune component models such as sticking, erosion and shedding.

A parametric study of Mach number, Total Water Content, relative humidity, particle size distribution and angle of angle of attack was performed. Backlit shadowgraphy of the stator tip was used to image the accretion profile throughout the test. Camera views onto the pressure and suction surfaces provided qualitative assessments of ice quality, spanwise uniformity and shedding behaviour. In some cases, the net sticking efficiency (defined as the net (measured) sticking mass flux as a fraction of the impinging mass flux) was compared to existing models. Specific conclusions may be summarized as:

1. Wet bulb temperature was varied in the range -6.5 °C to 5.5 °C by performing a sweep of relative humidity between 5% and 65% at a total temperature of 10 °C. Additional tests were performed at an elevated total temperature of 20 °C. A maximum leading edge ice growth rate was found at a bulk melt ratio of ~ 10%, in agreement with previous testing [3]. However, there was a steeper roll-off at higher melt ratios than previously observed, with negligible leading accretion at a melt ratio of ~ 18%. This highlights a geometry dependence at these slushy conditions, and reiterates the importance of developing robust sliding and shedding models. The growth rate of the second accretion (i.e. after the first shed) was found to be approximately equal between the 10 °C and 20 °C total temperature cases, attributed to surface cooling during the first accretion.
2. For tests where erosive condition (air velocity and particle size distribution) was varied, the reduction in leading edge growth rate was observed to correlate with the increasing bulk particle kinetic energy. Accretions generated at elevated particle sizes tended to initiate at the vane root, tip or trailing edge.
3. The vane angle of attack was varied between -20 ° and 20° in steps of 10 °. Positive angles of attack were observed to lead to high accretion growth rates across the pressure surface, attributed to the increased collection efficiency and reduced erosion rate (which is maximal for tangential particle impacts rather than normal impacts). Significantly reduced growth rates were observed for negative angles of attack, with accretions increasingly migrating to the suction surface. Low growth rates were attributed to (i) a generally low collection efficiency across the suction surface and (ii) its convex curvature, which is less likely to re-capture previously-bounced particles.
4. A qualitative assessment of shedding behaviour was performed, as a function of test condition. At high melt ratios, continual sliding of slushy accretions was observed, with little or no leading edge accretion. At moderate melt ratios (~ 10%, within the plateau region), accretions were more firmly hooked around the leading edge and had a reduced propensity to shed. Sheds that occurred during the test would typically be of a significant proportion of the accretion - e.g. the entire leading edge accretion or a portion of pressure surface accretion. The most stable accretions, which generally formed at melt ratios of ~7%, would only shed after the ice flow had ceased. At negative angles of attack, shedding was observed during the test, compared to no shedding in the positive angle of attack cases.

Contact Information

Corresponding author: Alexander Bucknell

Department of Engineering Science, Oxford Thermofluids Institute

alexander.bucknell@eng.ox.ac.uk

Acknowledgments

The authors would like to thank Rolls-Royce Plc for funding the research; the UK Engineering and Physical Sciences Research Council (EPSRC) for the CDT in Gas Turbine Aerodynamics studentship (grant ref. EP/L015943/1); and Trevor Godfrey, Gregory King and staff at the NRC Gas Turbine Laboratory for assistance in instrumenting the test article.

Appendices

Appendix A – Numerical Setup

Continuous Phase

The computational domain is a thin (5mm) 3D slice of the stator test article installed in RATFac, as shown in Fig. A-1. Using a 3D slice was found to aid convergence compared to a 2D case. Periodic

boundary conditions were applied on the side walls of the domain. Approximately eight chord lengths were modelled upstream of the blade; and the full tunnel height was used.

A hybrid tetrahedral-prism unstructured mesh was used. A grid independence study was performed, with a 2.3M cell grid selected based on < 0.5% difference in pressure surface shear stress compared to a finer grid.

The boundary layer mesh comprised 22 prism layers applied at solid boundaries. The maximum y+ on the stator surface up to 90% chord was 1.5. The solver was ANSYS Fluent v16.2, using density-based RANS. The k-ω SST turbulence model was used. Inlet boundary conditions were fixed at a total temperature of 283 K, total pressure of 34.5 kPa, and freestream Mach numbers of 0.25 & 0.40, matching the baseline aerodynamic conditions. The inlet turbulence intensity was set at 7.5% and the lengthscale at 0.08 m [9].

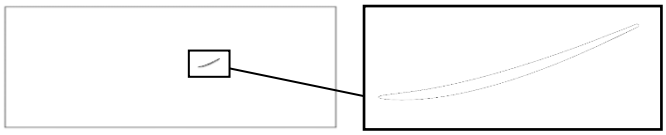


Fig. A1 Computational domain for stator test article, flow is left to right.

Discrete Phase Modelling

The in-built Lagrangian particle tracking in Ansys FLUENT v16.2 was used to calculate the particle trajectories through the domain.

Only drag was considered in the simulation; all other body forces (gravity, Saffman's lift force, Brownian force, thermophoresis and turbophoresis) were either at least two orders of magnitude smaller than the drag term or neglected since the particle Stokes number at the baseline test condition was > 10. The drag on a given particle at a given timestep was calculated using:

$$\vec{F}_{d,i} = -\frac{1}{2}\rho C_D\, A_{p,\perp}\, |\vec{u}_{p,i} - \vec{u}_i|(\vec{u}_{p,i} - \vec{u}_i) \qquad \text{(A1)}$$

where $A_{p,\perp}$ is the particle area projected normal to the direction of travel, $\vec{u}_i$ is the fluid velocity in the same direction, and C_D is the drag coefficient. The non-spherical particle drag coefficient of Haider & Levenspiel [15] was selected, using a mean particle aspect ratio found during previous particle morphology studies [16].

Particle tracking was performed as a post-processing step (i.e. one-way momentum coupling between fluid and particles). This was deemed acceptable since the particle mass loading at the baseline condition is significantly below unity [21], defined as

$$Z = {}^{TWC}/_{p_a} = 0.013 \qquad \text{(A2)}$$

The four particle size distributions used in the study were converted to equivalent Rosin-Rammler distributions. A Rosin-Rammler distribution is typically used to describe particles generated in sprays or comminution processes (cutting or grinding). The mass fraction of particles with diameter greater than d is given by

$$Y_d = e^{-(d/\bar{d})^n} \qquad \text{(A3)}$$

where $\bar{d}$ is the diameter constant, defined as the value of d at which $Y_d = e^{-1}$, and n is the spread parameter, given by

$$n = \frac{\ln(-ln(Y_d))}{\ln(d/\bar{d})} \qquad \text{(A4)}$$

The Rosin-Rammler parameters for each of the four PSDs used in the study are given in Table A1. An injection of 10,000 particles, generated from randomly sampling the Rosin-Rammler distribution, was found to achieve statistical convergence on the predicted collection efficiency distribution.

Table A1 Rosin-Rammler parameters for PSDs used in the study

Designation	D_{min} $[\mu m]$	D_{max} $[\mu m]$	n $[-]$	$\bar{d}$ $[\mu m]$
PSD 1 (baseline)	2	104	2.46	38.8
PSD 2	8	162	2.09	53.1
PSD 3	19	202	1.98	63.3
PSD 4	23	268	2.13	89.9

Appendix B – Uncertainty Analysis

The method of Moffat [22] is used to calculate the uncertainty in derived parameters from the root-sum-square of bias and precision uncertainties in measured parameters.

Measured Parameters

Table B1 shows bias (B) and precision (S) uncertainties of directly measured parameters for an example test run. The bias uncertainties quoted were either provided by the instrument manufacturer, by RATFac, or taken from [16] in the case of the PSD. The aerodynamic parameters are sampled pre- and post-test, at a rate of 10 Hz for a period of 30 s. Ice flow is then initiated, followed by insertion of the LWC-sensing SEA multiwire probe and TWC-sensing Compact Iso-Kinetic Probe (CIKP). These measurements are used to tune the icing conditions before the test is commenced; at least 150 samples are taken. The order of 10,000 particles are sampled for the PSD calculation. For the reasons stated in "Icing Cloud Calibration and Measurement", the uncertainty in the LWC measurement is not quantified here.

Table B1 Bias and precision uncertainties for measured parameters in an example test

		Uncertainty to 95% confidence		
Parameter	*Mean for run*	*Bias (B)*	*Precision (S)*	*Absolute (U)*
T_0 [°C]	10.8	1.0	0.018	1.0
P_0 [kPa]	34.7	0.030	0.0024	0.030
P_S [kPa]	33.3	0.030	0.0039	0.030
M [-]	0.245	0.0030	0.00023	0.030
TWC_{CIKP} [g/m^3]	8.04	0.40	0.081	0.41
RH [-]	0.462	0.0068	0.00064	0.0068
D_{v10} [µm]	14.4	0.72	0.11	0.73
D_{v50} [µm]	29.7	1.49	0.28	1.51
D_{v90} [µm]	52.9	2.65	1.19	2.90

Derived Parameters

For a variable W derived from directly measured parameters x, y, z, such that $W = f(x, y, z)$, the uncertainty in W is given by equation (B1) [22]:

$$U_W = \sqrt{\left(\frac{\partial W}{\partial x} U_x\right)^2 + \left(\frac{\partial W}{\partial y} U_y\right)^2 + \left(\frac{\partial W}{\partial z} U_z\right)^2} \quad \text{(B1)}$$

For the side view camera (viewing the blade tip), the physical ice thickness, h, is related to the its corresponding height in pixels, P, by

$$h = \frac{P}{S\ \cos(\alpha + \beta)} \quad ; \quad S = \frac{np}{L} \quad \text{(B2)}$$

where S is a conversion factor in pixels per mm. This is calculated using L, a physical length in the image, and the corresponding number of pixels, np. L is taken as the axial chord of the blade, which had an uncertainty of +/- 0.2 mm. α and β are the viewing angles of the camera relative to the vertical and lateral planes respectively. These were fixed at $\alpha = \beta$ = 0.0 +/- 0.2°, (i.e. a normal view), with the angle measured by a Mitutoyo 950 digital protractor.

The bias uncertainty in the thickness at any timestep t, $U_h(t)$, is then given by equation (B3), using $B_\alpha = B_\beta$:

$$B_h(t) = \sqrt{\left(\frac{\partial h}{\partial P} B_P\right)^2 + \left(\frac{\partial h}{\partial S} B_S\right)^2 + 2\left(\frac{\partial h}{\partial \alpha} B_\alpha\right)^2}$$
$$= \sqrt{\left(\frac{B_P}{S\cos(\alpha+\beta)}\right)^2 + \left(\left(\frac{-P(t)}{S^2\cos(\alpha+\beta)}\right)\left(\sqrt{\left(\frac{-np}{L^2}B_L\right)^2 + \left(\frac{1}{L}B_{np}\right)^2}\right)\right)^2 + 2\left(\frac{P(t)}{S}\sec(\alpha+\beta)\tan(\alpha+\beta)\,B_\alpha\right)^2} \quad \text{(B3)}$$

At the baseline test condition, the bias uncertainty at test start, $B_h(0)$ = +/-0.09 mm and at test end $B_h(180)$ = +/-0.18 mm. At discrete timepoints of each test, the amplitude of signal noise in the measured thickness was used to obtain an estimate of precision uncertainty. This proved to be highly dependent on test condition, with the combined precision and bias uncertainty estimated to be $U_h(180)$ = +/-1.0 mm in the worst case.

Thickness growth rate, $\dot{h}$, is calculated over a short time period δ (typically taken as 5 s), giving an absolute uncertainty of

$$U_{\dot{h}}(t) = \sqrt{\left(\frac{1}{\delta}U_h(t)\right)^2 + \left(\frac{1}{\delta}U_h(t+\delta)\right)^2 + \left(\frac{-h(t+\delta)+h(t)}{\delta^2}B_\delta\right)^2} \quad \text{(B4)}$$

The final stage is to calculate the uncertainty in net sticking efficiency (given by equation 3). Evaluating Equation B1 with respect to $\dot{h}$, γ, TWC and U_∞:

$$U_{\eta_{s,net}} = \sqrt{\left(\frac{K\ \sec(\gamma)}{TWC\ U_\infty}B_h(t)\right)^2 + \left(\frac{K\dot{h}\ \tan(\gamma)\sec(\gamma)}{TWC\ U_\infty}B_\gamma(t)\right)^2 + \left(\frac{-K\dot{h}\ \sec(\gamma)}{TWC^2 U_\infty}U_{TWC}\right)^2 + \left(\frac{-K\dot{h}\ \sec(\gamma)}{TWC {U_\infty}^2}U_{U_\infty}\right)^2} \quad \text{(B5)}$$

where $K = \rho_{acc}/\varepsilon_{loc}$.

The value of B_P, B_L, B_{np}, B_α, B_δ, U_{U_∞} and U_{TWC} are given in Table B2.

Table B2 Terms in equations (B3)-(B5) for calculating uncertainty in net sticking efficiency to 95% confidence

Term	*Uncertainty in…*	*Value*
B_P [pixels]	Ice accretion edge detection	2
B_L [mm]	Stator axial chord for length scale	0.2
B_{np} [pixels]	Number of pixels corresponding to known length	2
B_α [°]	Angle of camera / angle of attack	0.2
B_δ [s]	Time at which growth rate calculated. Taken as 1 camera frame	0.2
U_{U_∞} [m/s]	Velocity	1.01
U_{TWC} [g/m^3]	TWC	See Table B1

References

[1] J. G. Mason, J. W. Strapp, and P. Chow, 'The Ice Particle Threat to Engines in Flight', presented at the 44th AIAA Aerospace Sciences Meeting and Exhibit, Reno, Nevada, 2006.

[2] A. Bucknell, M. McGilvray, D. R. H. Gillespie, G. Jones, and B. Collier, 'A Model for Glaciated & Mixed Phase Icing for Application to Aircraft Engines', presented at the International Conference on Icing of Aircraft, Engines, and Structures, Minneapolis, MN, 2019.

[3] A. Bucknell, M. McGilvray, D. R. H. Gillespie, G. Jones, A. Reed, and B. Collier, 'Experimental Studies of Ice Crystal Accretion on an Axisymmetric Body at Engine-Realistic Conditions', presented at the 2018 Atmospheric and Space Environments Conference, Atlanta, GA, USA, 2018.

[4] T. Currie, D. Fuleki, and A. Mahallati, 'Experimental Studies of Mixed-Phase and Sticking Efficiency for Ice Crystal Accretion in Jet and Engines', presented at the 6th AIAA Atmospheric and Space Environments Conference, Atlanta, GA, 2014.

[5] P. M. Struk, T. Bartkus, and Tsao J., 'Ice Accretion Measurements on an Airfoil and Wedge in Mixed-Phase Conditions', *SAE Technical Paper 2015-01-2116*, 2015.

[6] J. G. Mason, P. Chow, and D. M. Fuleki, 'Understanding Ice Crystal Accretion and Shedding Phenomenon in Jet Engines Using a Rig Test', *Journal of Engineering for Gas Turbines and Power*, vol. 133, no. 4, pp. 041201 1–8, Apr. 2011.

[7] D. C. Knezevici, D. M. Fuleki, T. C. Currie, and J. D. MacLeod, 'Particle Size Effects on Ice Crystal Accretion', presented at the 4th AIAA Atmospheric and Space Environments Conference, New Orleans, Louisiana, USA, 2012.

[8] P. M. Struk and C. J. Lynch, 'Ice Growth Measurements from Image Data to Support Ice-Crystal and Mixed-Phase Accretion Testing', presented at the 4th AIAA Atmospheric and Space Environments, New Orleans, Louisiana, USA, 2012.

[9] D. C. Knezevici, D. Fuleki, and J. MacLeod, 'Development and Commissioning of a Linear Compressor Cascade Rig for Ice Crystal Research', *SAE Technical Paper 2011-38-0079*, Jun. 2011.

[10] P. M. Struk *et al.*, 'Fundamental Ice Crystal Accretion Physics Studies', presented at the SAE 2011 International Conference on Aircraft and Engine Icing and Ground Deicing, Chicago, IL, USA, 2011.

[11] C. Davison, C. Landreville, and M. Benner, 'Development and Validation of Compact Isokinetic Total Water Content

Probe for Wind Tunnel Characterization', presented at the 8th AIAA Atmospheric and Space Environments Conference, Washington, D.C., USA, 2016.
[12] L. Lilie, E. Emery, J. Strapp, and J. Emery, 'A Multiwire Hot-Wire Device for Measurement of Icing Severity, Total Water Content, Liquid Water Content, and Droplet Diameter', presented at the 43rd AIAA Aerosp. Sci. Meet. Exhib., 2005.
[13] P. M. Struk *et al.*, 'An Initial Study of the Fundamentals of Ice Crystal Icing Physics in the NASA Propulsion Systems Laboratory', presented at the 9th AIAA Atmospheric and Space Environments Conference, Denver, Colorado, 2017.
[14] J. Canny, 'A Computational Approach To Edge Detection', presented at the IEEE Transactions of Pattern Analysis and Machine Intelligence, 1986, vol. 8(6), pp. 679–698.
[15] A. Haider and O. Levenspiel, 'Drag Coefficient and Terminal Velocity of Spherical and Nonspherical Particles', *Powder Technology*, vol. 58, no. 1, pp. 63–70, 1989.
[16] D. Fuleki, J. L. Chalmers, and B. Galeote, 'Technique for Ice Crystal Particle Size Measurements and Results for the National Research Council of Canada Altitude Ice Crystal Test System', *SAE Technical Paper 2015-01-2125*, 2015.
[17] P. M. Struk *et al.*, 'Ice Crystal Icing Physics Study using a NACA 0012 Airfoil at the National Research Council of Canada's Research Altitude Test Facility', presented at the 2018 Atmospheric and Space Environments Conference, Atlanta, GA, USA, 2018.
[18] I. Day, J. Williams, and C. Freeman, 'Rain Ingestion in Axial Flow Compressors at Part Speed', *ASME Journal of Turbomachinery*, vol. 130, Jan. 2008.
[19] P. Guégan *et al.*, 'Experimental investigation of the kinematics of post-impact ice fragments', *International Journal of Impact Engineering*, vol. 38, pp. 786–795, 2011.
[20] T. Hauk, I. Roisman, and C. Tropea, 'Investigation of the Impact Behaviour of Ice Particles', *6th AIAA Atmospheric and Space Environments Conference 16-20 June 2014, Atlanta, GA*, 2014.
[21] W. B. Wright, P. C. E. Jorgenson, and J. P. Veres, 'Mixed Phase Modeling in GlennICE with Application to Engine Icing', presented at the AIAA Atmospheric and Space Environments Conference, Toronto, Ontario Canada, 2010.
[22] R. Moffat J., 'Describing the Uncertainties in Experimental Results', *Experimental Thermal and Fluid Science*, vol. 1, no. 1, pp. 3–17, 1988.

Nomenclature

Latin		
C	Stator true chord	m
$D_{v,xx}$	Diameter for which all particles with $D < D_{v,xx}$ constitute xx% of the total volume	μm
FR	False response (of multiwire probe)	-
$\dot{h}$	Ice growth rate	m/s
i	Angle of attack/incidence	°
KE	Kinetic energy parameter	m^5/s^2
L	Characteristic length	m
LWC	Liquid Water Content	g/m^3
$\dot{m}$	Mass flux	$kg/(s.m^2)$
m	Mass	kg
MR	Melt ratio	-
P	Pressure	Pa
RH	Relative humidity	-
s	Surface coordinate on stator	m
t	Time	s
T	Temperature	℃
TAT	Total Air Temperature	℃
Twb	Wet bulb temperature	K
TWC	Total Water Content	g/m^3
T_f	Freezing temperature of water	℃
U	Velocity	m/s
Greek		
β	Collection efficiency	-
γ	Angle from surface normal to axial	-
ε	Ballistic efficiency	-
η	Efficiency (sticking, erosion)	
ρ	Density	kg/m^3

Subscripts	
0	Total or baseline (KE)
∞	Freestream
a	Air
acc	Accretion
$CIKP$	Compact Iso-Kinetic Probe
cl	Centreline
ero	Erosion
imp	Impinging (particles)
loc	Local
$MW, multi$	SEA multiwire probe
s	Sticking
x	Axial direction
Groups	
M	Mach number = $U/\sqrt{\gamma_f R_f T}$
Re_p	Particle Reynolds number = $\rho U_{rel} D_p/\mu_f$